NPG Asia Materials (2012) 4, e6; doi:10.1038/am.2012.10
© Nature Japan K.K. All rights reserved 1884-4057/12
www.nature.com/am

ORIGINAL ARTICLE

Tunable and sizable band gap of single-layer graphene sandwiched between hexagonal boron nitride

Ruge Quhe[1,2,5], Jiaxin Zheng[1,2,5], Guangfu Luo[1,3,5], Qihang Liu[1], Rui Qin[1], Jing Zhou[1], Dapeng Yu[1], Shigeru Nagase[3], Wai-Ning Mei[4], Zhengxiang Gao[1] and Jing Lu[1]

Opening a tunable and sizable band gap in single-layer graphene (SLG) without degrading its structural integrity and carrier mobility is a significant challenge. Using density functional theory calculations, we show that the band gap of SLG can be opened to 0.16 eV (without an electric field) and 0.34 eV (with a strong electric field) when properly sandwiched between two hexagonal boron nitride single layers. The zero-field band gaps are increased by more than 50% when the many-body effects are included. The *ab initio* quantum transport simulation of a dual-gated field effect transistor (FET) made of such a sandwich structure reveals an electric-field-enhanced transport gap, and the on/off current ratio is increased by a factor of 8.0 compared with that of a pure SLG FET. The tunable and sizeable band gap and structural integrity render this sandwich structure a promising candidate for high-performance SLG FETs.
NPG Asia Materials (2012) **4,** e6; doi:10.1038/am.2012.10; published online 17 February 2012

Keywords: density functional theory; electric field; graphene; h-BN sheet; quasiparticle correction; transport properties

INTRODUCTION

Despite its extremely high carrier mobility (1. $5\times10^4\,cm^2\,V^{-1}\,s^{-1}$ for a SiO_2-supported sample[1] and $2\times10^5\,cm^2\,V^{-1}\,s^{-1}$ for a suspended sample[2,3]), pristine graphene cannot be used for effective room-temperature field effect transistors (FET) because of its zero band gap. Opening and tailoring a band gap in graphene is probably one of the most important and urgent research topics in the graphene research currently. A large number of methods have been developed to open a band gap in graphene, and these methods can be classified into the following two types, depending on whether they preserve the integrity of the honeycomb structure: in a type I method, the honeycomb structure is destroyed, and in a type II method, the honeycomb structure of graphene is preserved. Typical type I methods include cutting graphene into nanoribbons,[4] making graphene nanomeshes,[5] and chemical functionalization.[6,7] The main disadvantage of the type I methods is that the carrier mobility and on-state current are greatly reduced because the destruction of the honeycomb structure introduces scattering centers, enhances the carrier effective mass and produces a non-tunable band gap.

Unlike the type I method, high carrier mobility can be maintained in the type II method because the honeycomb structure is maintained. Typical type II methods include graphene–substrate interaction[8,9] and the application of strain.[10] The graphene band gap induced by a substrate is not tunable. The most effective type II method is the application of an external electric field to the graphene. Both theoretical calculations and experiments show that a vertical external electric field can induce a tunable band gap of up to 0.25 eV for bilayer graphene (BLG)[11–13] because it breaks the inversion symmetry of BLG, and the carrier mobility is not significantly affected by the vertical electric field.[13] The mechanism of opening a BLG band gap by strain[10] is the generation of an equivalent vertical electric field by different strains on two layers. Unfortunately, this electric field scheme cannot be directly applied to single-layer graphene (SLG) because the two sublattices of SLG remain equivalent under the vertical electric field. Therefore, it is highly desirable to develop an effective method to open a tunable and sizable band gap for SLG without significant loss of carrier mobility, as can be done for BLG.

The common substrate for graphene FETs is SiO_2, whose charged surface state, impurities, rough surface and surface optical phonons limit the carrier mobility of the graphene. Recently, graphene has been transferred to hexagonal boron nitride (h-BN). The measured mobility of graphene on the h-BN substrate is comparable to that of suspended graphene, and it is one order of magnitude larger than that of SiO_2-supported graphene because the atomically flat h-BN substrate is free from dangling bonds and charge impurities.[14] A combination of the vertical electric field and the h-BN substrate is likely to be one development direction for future high-performance graphene FET devices. To this end, graphene should be sandwiched between h-BN. Recent theoretical calculations reveal that the electric field response of BLG sandwiched between h-BN is similar to that of

[1]State Key Laboratory of Mesoscopic Physics and Department of Physics, Peking University, Beijing, PR China; [2]Academy for Advanced Interdisciplinary Studies, Peking University, Beijing, PR China; [3]Department of Theoretical and Computational Molecular Science, Institute for Molecular Science, Okazaki, Japan and [4]Department of Physics, University of Nebraska at Omaha, Omaha, NE, USA
[5]These authors contributed equally to this work.
Correspondence: Professor J Lu, State Key Laboratory of Mesoscopic Physics and Department of Physics, Peking University, Chengfu Road, Beijing 100871, PR China.
E-mail: jinglu@pku.edu.cn
Received 7 September 2011; revised 29 November 2011; accepted 7 December 2011

freestanding BLG. However, there is a great discrepancy in calculations of the electric field tunability of SLG between h-BN. By using the tight-binding method, Sławińska *et al.*[15] show that an electric field can induce a tunable band gap of 0 eV (at zero field) to 0.23 eV for an *ABC*-stacked SLG between an h-BN single-layer sandwich, but the later density functional theory (DFT) calculation by Ramasubramaniam *et al.*[16] finds that the band gaps are insensitive to electric field for three *ABC*-stacked and three *ABA*-stacked h-BN/SLG/h-BN sandwich structures, and the largest band gap is merely 0.1 eV. Therefore, the existence of a tunable and sizable band gap in an h-BN/SLG/h-BN sandwich structure remains unverified, and additional extensive and intensive theoretical works are required to provide guidance for future device design based on h-BN/SLG/h-BN sandwich structures.

It has been well established that many-body effects significantly alter the electronic structure of a low-dimensional system because of the enhanced Coulomb interaction with the reduced dimension.[17,18] For example, the band gap of single-layer graphane (fully hydrogenated SLG) increases from 3.4 to 5.4 eV when many-body effects are included.[19] It is important to correct the DFT band gap of a two-dimensional h-BN/SLG/h-BN sandwich by taking many-body effects into account. So far, the quasiparticle band structure of an h-BN/SLG/h-BN sandwich has not been examined.

The ultimate application of SLG with an open band gap is the fabrication of an FET; thus, a transport property investigation is desired for an h-BN/SLG/h-BN sandwich under a vertical electric field. To this end, dual gates are required to provide a vertical electric field, in addition to control of the doping level. To the best of our knowledge, the transport properties (especially the switching effects) of an h-BN/SLG/h-BN sandwich under a vertical electric field are unknown.

In this article, we provide the first comprehensive investigation of the h-BN/SLG/h-BN sandwich structure by various theoretical methods. All 12 possible symmetric stacking modes are considered. The geometric and electronic properties and stability of these stacking modes are calculated by the DFT method, which is followed by a correction for the electronic structures, including many-body effects (*GW* approximation). The DFT coupled with the nonequilibrium Green's function is used to calculate the transport properties under a vertical electric field. We reveal that a band gap is opened for SLG in all stacking modes, with values ranging from 0.02∼0.16 eV. The band gaps of two stacking modes are insensitive to the vertical electric field, four stacking modes are sensitive to a unidirectional electric field and six stacking modes are sensitive to a bidirectional electric field. The band gaps of the eight stacking modes can be increased to over 0.30 eV under a strong electric field. The maximum zero-field band gap of the h-BN/SLG/h-BN sandwich is corrected to 0.23 eV after the many-body effects are considered. We simulate a dual-gated FET device from the h-BN/SLG/h-BN sandwich, and an electric-field-enhanced transport gap is confirmed, accompanied by an increase in the on/off current ratio by a factor of 8.0 over that of an SLG FET. Therefore, a tunable and sizable band gap, a transport gap and significant switching effects are well established for the first time in an h-BN/SLG/h-BN sandwich. Finally, we envision a route to realize a partially lattice-matched h-BN/SLG/h-BN sandwich device based on existing techniques. Our work is expected to stimulate the experimental realization of a high-performance h-BN/SLG/h-BN heterostructure FET.

MATERIALS AND METHODS

We perform DFT calculations within the local density approximation (LDA) to the exchange-correlation functional. The geometrical and electronic structures are calculated with the all-electron double numerical atomic orbital plus polarization (DNP)[20] basis set, which is implemented in the DMol^3 package.[20,21] A 36×36×1 Monkhorst–Pack *k*-point mesh[22] is applied to the Brillouin zone integration. The geometry optimization is performed for both the atomic position and the interlayer distance, until the maximum force on each atom is <0.01 eV/Å. The optimized interlayer distance of the BLG is 3.32 Å, which is in good agreement with the experimental value of 3.34 Å for graphite.[23] In our calculations, an electric field with strength ranging from −1 to 1 V/Å is applied along the direction perpendicular to the graphene plane. The electric field responses of three configurations are also calculated by the plane wave (PW) basis set and the projector-augmented wave (PAW) pseudopotential implemented in the VASP package.[24] A PW energy cutoff of 500 eV and a 45×45×1 Monkhorst–Pack *k*-mesh[22] are used to generate the charge densities. The atomic positions are relaxed by a conjugate gradient algorithm with a force tolerance of 0.01 eV/Å. The electric fields are applied perpendicular to the slabs by introducing dipolar sheets at the center of the simulation cell.

The quasiparticle calculations are carried out using the ABINIT package.[25] First, we compute the wave functions using DFT. A PW energy cutoff of 380 eV is used, together with the PAW pseudopotentials,[26] and the Brillouin zone is sampled with an 18×18×1 Monkhorst–Pack grid.[22] (A convergence test shows that a 42×42×1 Monkhorst–Pack grid calculation gives nearly the same band gap). Second, the quasiparticle energies E_{nk} are calculated using the following quasiparticle Schrödinger equation, which uses the self-energy Σ acquired from the *GW* approximation.[27]

$$\left[-\frac{\nabla^2}{2}+V_{\text{ion}}+V_{\text{Hartree}}+\sum(E_{nk})\right]\Psi_{nk}=E_{nk}\Psi_{nk} \quad (1)$$

Therein, the Green function and the Coulomb screening are constructed from the LDA results in the first step,[28] and the plasmon–pole model is used for the screening computation. We perform the *GW* calculation in a nonself-consistent way.

The first-principles quantum transport calculations, which are based on DFT and the nonequilibrium Green's function method, are performed using the ATK 11.2 package.[29,30] The single-zeta basis set is employed, and the temperature is set to 300 K. The effect of the gates is calculated by solving the Poisson equation self-consistently, instead of simply shifting the central region's chemical potential. The top gate and bottom gate voltages were defined as V_t and V_b. The distance between the two gates was d_0=26 Å in our model, and the thickness of the two identical dielectric regions is d_i=7 Å. The dielectric constant of the dielectric region is 3.9, which models SiO_2. The following vertical electric field applied to the sandwich structure is obtained: $E_\perp=\frac{V_b-V_t}{(d_0-2d_i)+2d_i/\varepsilon}$. The corresponding total gate voltage is V_g=V_t+V_b, which reflects the total doping level.

The DMol^3 and ATK packages use the atomic orbital basis set, while the VASP and ABINIT packages take the plane-wave basis set. To check the consistency between the results in the different basis sets and packages, we compared the zero-field band structures of Configuration **3** in Figure S1 of the Supplementary Information. These electronic structures from different basis sets and packages are basically similar, except for the single-zeta basis set in the ATK package (a larger basis set, for example, the DZP basis set, is not applicable to this transport calculation based on a very large system, but the determination of the electric-field-enhanced on/off current ratio should be qualitatively unchanged[31]), and the band gaps are nearly equal. The calculated band gaps of Configuration **3** are 0.098 (ABINIT), 0.108 (DMol^3), 0.100 (ATK), 0.100 (VASP obtained by us) and 0.090 eV (VASP obtained by Ramasubramaniam *et al.*[16]).

RESULTS

DFT electronic structure

A supercell is constructed for the sandwich structure of a single layer of graphene that is inserted between two h-BN single layers. We assume that the graphene and h-BN single layers are commensurate and that each supercell contains one unit cell of the graphene and one of each h-BN single layer because the lattice mismatch between the graphene and the h-BN single layer is <2%. The lattice constant of this sandwich structure is taken from that of graphene, a=b=2.445 Å.

The lattice constant along the direction perpendicular to the graphene plane is taken to be 30 Å. In graphite, the hexagonal graphene layers are reported to have three different stacking models: *AA*, *AB* and *ABC* stacking.[32] In our tri-layer sandwich structure, we consider four stacking models: *AAA*, *AAB*, *ABA* and *ABC* stackings. Because of the nonequivalence of the B and N sublattices of the h-BN single layer, we have 12 different configurations in total (Figure 1).

The h-BN/SLG/h-BN sandwich structure is characterized by both the stacking sequence of its layers and the positions of the C atoms relative to the B and N atoms of the bottom and top BN layer. For example, $ABC(\otimes\alpha\mathrm{B},\mathrm{N}\beta\otimes)$ means that the stacking sequence is *ABC*; a hexagonal ring center (labeled by ⊗) and a B atom are located directly below and above the C atom of the α sublattice, respectively; and a N atom and a hexagonal ring center are located directly below and above the C atom of β sublattice, respectively. The graphene/h-BN bilayer is described using similar notation in this study. For clarity, the 12 sandwich structures in this paper are also identified by each figure number in Figure 1.

There is no obvious buckling of either the graphene or h-BN single layers after optimization. The interlayer distances *d* between the graphene and the adjacent h-BN single layers in the sandwich structures range from 3.20 to 3.44 Å (see Figure 1). The relative stability (E_r), which is defined as the energy difference between the checked configuration and Configuration **12**, is shown in Figure 2 in descending order. Configurations **1** and **2** are the two most stable configurations. The binding energy E_b of the graphene/h-BN multilayer system is defined as the energy difference between the multilayer and the isolated single layers, as follows:

$$E_b = E - N_G \times E_G - N_{BN} \times E_{BN} \quad (2)$$

where E, E_G and E_{BN} are the total energies per unit cell of the multilayer, graphene and h-BN single layer, respectively; N_G and N_{BN} are the numbers of the graphene and the h-BN single layers, respectively; and E_b of the sandwich structures ranges from −0.123 to −0.168 eV per unit cell. Configurations **1** and **2** are the most and second most stable configurations, with binding energies of −0.1684 and −0.1683 eV per unit cell, respectively. We also calculate E_b of the graphene/h-BN bilayer, and the resulting E_b values for the $AB(\mathrm{B}\alpha,\otimes\beta)$, $AB(\mathrm{N}\alpha,\otimes\beta)$ and $AA(\mathrm{B}\alpha,\mathrm{N}\beta)$ configurations (for simplicity, we label them Configurations **I**, **II** and **III**, respectively) are −0.074, −0.054 and −0.052 eV per unit cell, respectively. This stability order is the same as that of the previous work.[33] It is found that E_b(sandwich structure) ≈ E_b(graphene/top h-BN layer) + E_b(graphene/bottom h-BN layer) − 0.020 eV per unit cell. As the bilayer configurations of the graphene/top h-BN and graphene/bottom h-BN are both $AB(\mathrm{B}\alpha,\otimes\beta)$ for Configuration **1** ($ABA(\mathrm{B}\alpha\mathrm{B},\otimes\beta\otimes)$) and **2** ($ABC(\otimes\alpha\mathrm{B},\mathrm{B}\beta\otimes)$), Configurations **1** and **2** are the two most stable

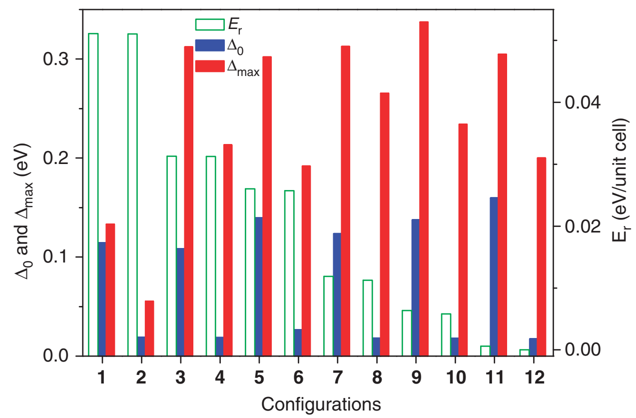

Figure 2 Relative stability, E_r, band gap under zero bias, Δ_0, and the maximum band gap under $E_\perp = -1$ to 1 V/Å, Δ_{max}, of the 12 single-layer graphene sandwich configurations calculated at the LDA level with the DNP basis set. The data are arranged according to decreasing stability.

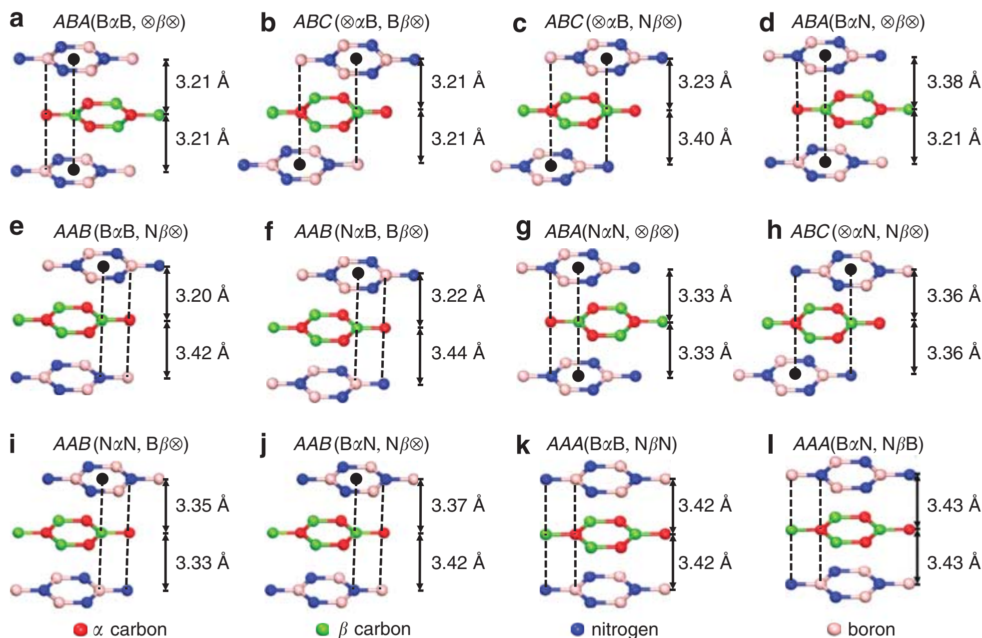

Figure 1 (**a**–**l**) Schematic models of the 12 configurations of single-layer graphene sandwiched between two h-BN single layers, respectively. The configurations are arranged in order of decreasing stabilities. *A*, *B* and *C* denote the three relative positions of the layers. Optimized interlayer distances between graphene and the adjacent h-BN single layer are indicated.

sandwich structures. We can express this relation simply as $E_b(\mathbf{1}) \approx E_b(\mathbf{2}) \approx 2E_b(\mathbf{I}) - 0.020$ eV per unit cell. As the bilayer configurations of the graphene/top h-BN and the graphene/bottom h-BN are both AA(Bα,Nβ) for Configurations **11** (AAA(BαB,NβN)) and **12** (AAA(BαN,NβB)), Configurations **11** and **12** are the two least stable sandwich structures. We can express this relation as $E_b(\mathbf{11}) \approx E_b(\mathbf{12}) \approx 2E_b(\mathbf{III}) - 0.020$ eV per unit cell. Similarly, the following four additional relations are identified: $E_b(\mathbf{3}) \approx E_b(\mathbf{4}) \approx E_b(\mathbf{I}) + E_b(\mathbf{II}) - 0.020$ eV per unit cell, $E_b(\mathbf{5}) \approx E_b(\mathbf{6}) \approx E_b(\mathbf{I}) + E_b(\mathbf{III}) - 0.020$ eV per unit cell, $E_b(\mathbf{7}) \approx E_b(\mathbf{8}) \approx 2E_b(\mathbf{II}) - 0.020$ eV per unit cell and $E_b(\mathbf{9}) \approx E_b(\mathbf{10}) \approx E_b(\mathbf{II}) + E_b(\mathbf{III}) - 0.020$ eV per unit cell. As $2E_b(\mathbf{I}) < E_b(\mathbf{I}) + E_b(\mathbf{II}) < E_b(\mathbf{I}) + E_b(\mathbf{III}) < 2E_b(\mathbf{II}) < E_b(\mathbf{II}) + E_b(\mathbf{III}) < 2E_b(\mathbf{III})$, we have $E_r(\mathbf{1}) \approx E_r(\mathbf{2}) > E_r(\mathbf{3}) \approx E_r(\mathbf{4}) > E_r(\mathbf{5}) \approx E_r(\mathbf{6}) > E_r(\mathbf{7}) \approx E_r(\mathbf{8}) > E_r(\mathbf{9}) \approx E_r(\mathbf{10}) > E_r(\mathbf{11}) \approx E_r(\mathbf{12})$, and this order is in good agreement with the strict calculations.

Configurations with similar stabilities always come in pairs. A close examination of each pair of configurations in this study shows that the chemical environments for the carbon atoms in those paired configurations were nearly identical when the α and β carbon atoms are considered as a whole. For example, in the paired Configurations **1** and **2,** there is a B atom and a hexagonal ring center (⊗) both above and below the carbon atoms, and we express this similar chemical environment as (B⊗αβ⊗B).

The direct band gaps at the K point are opened for all of the configurations under zero field. The zero-field electronic structures of Configurations **1**, **3** and **11** are shown in Figures 3a, b and c by blue lines, with zero-field band gap (Δ_0) of 0.115, 0.108 and 0.160 eV, respectively. The Δ_0 values of the 12 configurations are presented in Figure 2, and they can be categorized into two groups according to their size. Group I includes Configurations **1**, **3**, **5**, **7**, **9** and **11**, while Group II includes Configurations **2**, **4**, **6**, **8**, **10** and **12**. The BN layers introduce different chemical environments for the α and β carbon atoms in group I, while in group II, the environments of the α and β carbon atoms are similar. Thus, the values of Δ_0 in group I (0.108–0.160 eV) are significantly greater than those in group II (0.017–0.026 eV), and the values of Δ_0 in group I are two to three times those (~0.05 eV) of the graphene/h-BN bilayer.[33]

To understand the nature of the difference between the two groups, an orbital interaction model is employed. In this model, only the interactions between the π orbitals of the adjacent atoms are considered. According to their electronegativity, one has $E_B > E_C > E_N$, where E_i (i=B, C, or N) is the energy level of the orbital of the i atom. Δ_{C-i} (>0) is the energy level splitting due to the interaction between the C and the i atoms. In Configurations **1** and **2**, which are from group I and group II, respectively, E_B is degenerated in the top and bottom BN layers at zero field (Figure 4a and b). The coupling between the two B atoms and the C atom of the α sublattice in Configuration **1** shifts the energy level of the α carbon atom downward. This new energy level of the α carbon atom ($E_\alpha = E_C - 2\times\Delta_{C-B}$) acts as the valence band maximum, in which Δ_{C-B} is the energy level splitting caused by the coupling between the C and either B atoms. A pair of hexagonal ring centers are located directly below and above the C atom of the β sublattice; thus, the energy level of the β carbon atom ($E_\beta = E_C$) remains constant and acts as a conduction band minimum. The resulting band gap, which is the energy level difference between the α and β carbon atoms ($\Delta_0 = E_\alpha > E_\beta$), is $\sim 2\times\Delta_{C-B}$. The shifted energy levels of the two carbons in Configuration **2**, shown in Figure 4b, are approximately equal ($E_\alpha \approx E_\beta$) because both the α and β carbon atoms are coupled with a B atom. For this reason, it is difficult to open a band gap in Configuration **2**. Generally, the BN layers break the symmetry between the α and β carbon atoms for group I, but not for group II. The energy splitting between E_α and E_β in group I leads to an obvious band gap. However, in group II, the energy levels of the two carbon atoms shift in a similar way ($E_\alpha \approx E_\beta$), and the resulting band gaps are quite small.

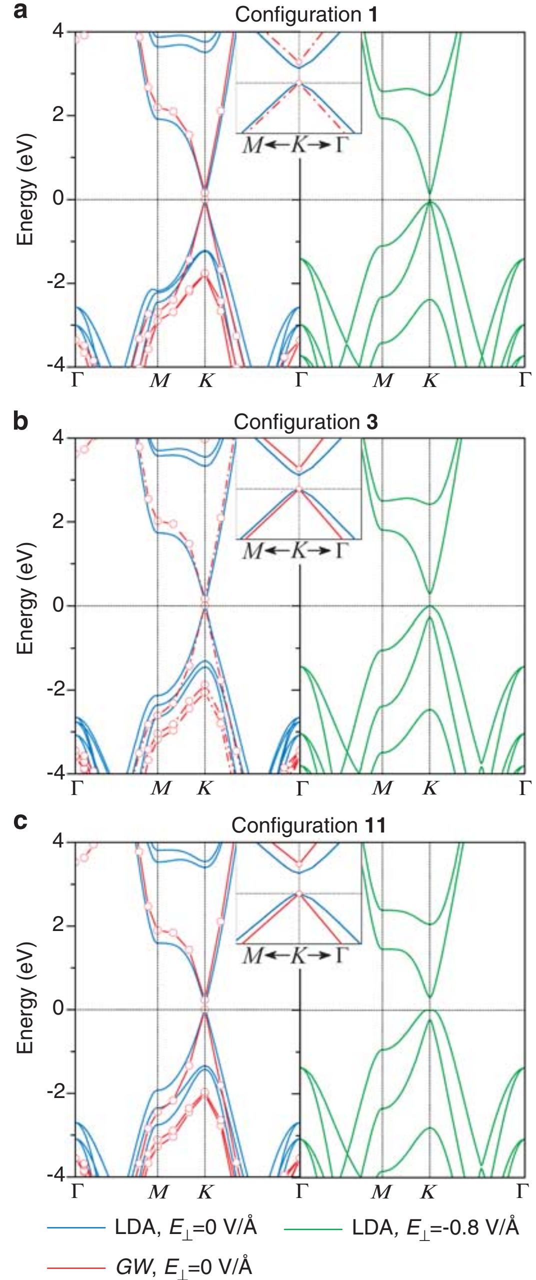

Figure 3 Band structures of (**a**) Configuration **1**, (**b**) Configuration **3** and (**c**) Configuration **11** at the LDA/DNP level with (blue line) and without $E_\perp$ (green line), and at the GW/PW level without $E_\perp$ (red circle). Insets: band structures near the Fermi level at the LDA/DNP and GW/PW levels. The red-dashed lines connecting the red circles are guidance for the eye. The valence band maximum is set to zero.

The electric field causes a change in the band structure of the sandwiches. The electronic structures of Configurations **1**, **3** and **11** under $E_\perp = -0.8$ V/Å are shown by green lines in Figures 3a–c, respectively, and their band gaps are increased by 0.02, 0.18 and 0.15 eV, respectively, with respect to their zero-field values. The maximum band gaps (Δ_{max}) under the investigated electric field

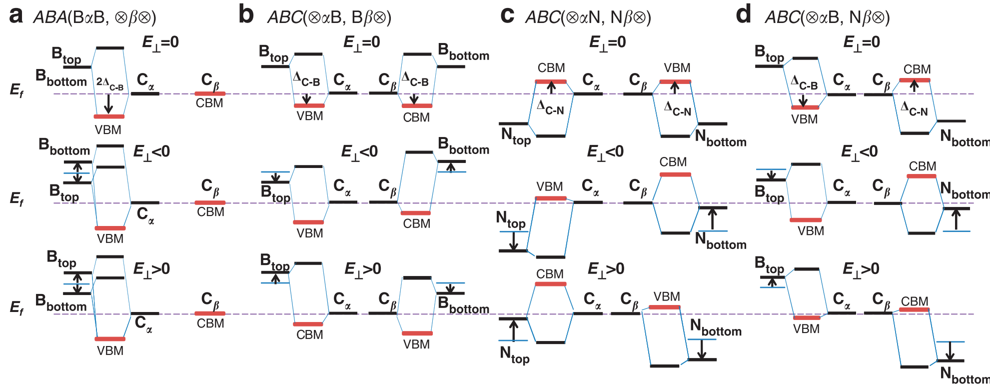

Figure 4 (**a**–**d**) Schematic energy diagram for (**a**) Configuration **1**, (**b**) Configuration **2**, (**c**) Configuration **7** and (**d**) Configuration **3** under zero, negative and positive electric field, respectively. B_{top}, N_{bottom}, C_{α}, and C_{β} denote B atoms at the top h-BN single layer, N atoms at the bottom h-BN single layer and C atoms at the α and β sublattices of graphene, respectively.

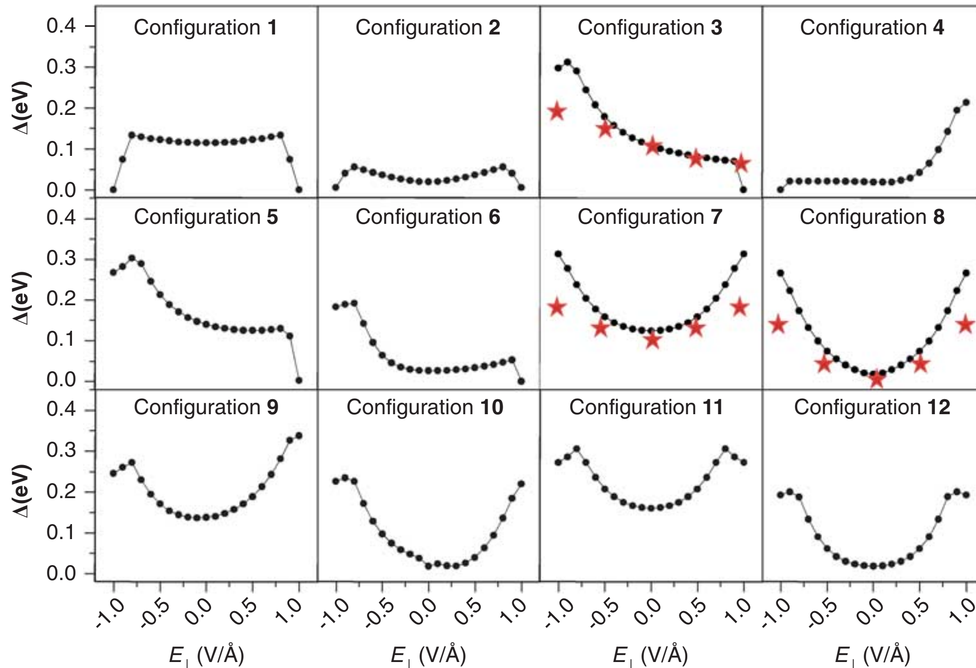

Figure 5 Band gaps of the 12 single-layer graphene sandwich configurations as a function of the electric field strength obtained at the LDA/DNP level (black dot) and LDA/PW (red star) level. The data are arranged according to decreasing stability.

range ($E_{\perp}$) of the 12 sandwich structures are shown in Figure 2, with values ranging from 0.056 to 0.337 eV. Most of the maximum band gaps occur at the *K* point. Remarkably, the Δ_{max} values of eight configurations exceed 0.2 eV. In contrast, the maximum band gap under $E_{\perp}$ in a graphene/h-BN bilayer is only 0.13 eV.[33]

The $E_{\perp}$ dependences of the band gaps of the entire set of sandwich structures are displayed in Figure 5, and the positive direction is defined as the direction from the bottom to the top layer. The structures can be classified into two groups by their symmetry with respect to the electric field direction: a symmetric group (Configurations **1**, **2**, **7**, **8**, **11** and **12**) and an asymmetric group (Configurations **3**, **4**, **5**, **6**, **9** and **10**) with respect to $E_{\perp}$. This phenomenon can also be explained by our orbital interaction model. The potential energy arising from the external electric field was set to zero at the middle graphene layer. Figures 4a and d show the electric-field-dependent schematic energy diagrams of Configurations **1** and **3**, which belong to the symmetric group and the asymmetric group, respectively. In Configuration **1**, a negative $E_{\perp}$ causes E_B in the bottom and top layers to shift upward and downward, respectively. Under a positive $E_{\perp}$, E_B in the bottom and top layers shifts downward and upward, respectively. The valence band maximum, and thus the band gap, is independent of the direction of $E_{\perp}$ in Configuration **1**. In contrast, under a negative $E_{\perp}$, both E_B and E_N move toward E_C in Configuration **3**, reducing the band gap from its value at Δ_0. When $E_{\perp}$ is changed to the positive direction, both E_B and E_N diverge from E_C, enhancing the band gap from its value at Δ_0. Therefore, the electric dependence of Δ is asymmetric about the electric field direction. By comparing Configurations **1** and **2** with **7** and **8** in Figure 5, it can be seen that the band gap is much larger if the B atoms are changed to N atoms under a given electric field. E_N exhibits greater divergence than E_B with an applied electric field, as illustrated in Figures 4b and c.

Configurations **2** and **8** are studied by Sławińska *et al.*[15] with the tight-binding approach. Under an electric field, a tunable band gap as large as 0.23 eV is opened for Configuration **8**, while the band gap of Configuration **2** is insensitive to electric field. Their results are in agreement with our DFT calculation, except that the Δ_0 is 0.02 eV in our DFT calculation, but it vanishes when calculated with the tight-binding method. A DFT calculation by the same authors also obtains a band gap of 0.23 eV under a strong electric field.[15] The following six configurations are checked by Ramasubramaniam *et al.*,[16] using the DFT method with the PW basis set and the PAW pseudopotentials implemented in the VASP package: Configurations **1**, **2**, **3**, **4**, **7** and **8**. Compared with our DFT calculations using the DNP basis set,[20] Ramasubramaniam *et al.*[16] found the same zero-field gaps (the relative difference is $<10^{-2}$ eV) but different electric field responses. They found that the band gaps of these six tri-layer structures are either entirely non-tunable or slightly tunable, even if the electric field reaches 0.5 V/Å, and the largest band gap attainable is 0.1 eV. However, in our DFT calculations, the band gaps of three of their six checked configurations (Configurations **3**, **7** and **8**) are sensitive to an electric field, changing by 0.071, 0.056 and 0.035 eV, respectively, when the electric field strength is 0.5 V/Å.

One possible cause of this discrepancy is the failure to consider the dependence of the band gaps on the direction of $E_\perp$ in the previous work. A negative $E_\perp$ is necessary to open a sizable band gap in Configuration **3**. Under a positive $E_\perp$ of <0.5 V/Å, the band gap of Configuration **3** is also insensitive to an electric field in our calculation. Another possible cause of the discrepancy is the difference in the basis set and package. To examine this possibility, we calculate the electric field response of Configurations **3**, **7** and **8** using the PW basis set and the PAW pseudopotential implemented in the VASP package, and we use calculation parameters consistent with the work of Ramasubramaniam *et al.*[16] As shown in Figure 5, the resulting band gap responses of Configurations **7** and **8** to $E_\perp$ are less than those in the DMol^3 calculations, but they are larger than those obtained by Ramasubramaniam *et al.*[16] The band gaps of Configurations **7** and **8** increase by 0.02 and 0.04 eV, respectively, relative to Δ_0 under $E_\perp$=0.5 V/Å, and they increase by 0.07 and 0.13 eV, respectively, relative to Δ_0 if $E_\perp$ reaches 1 V/Å. The monotonic change of the band gap with $E_\perp$ for Configuration **8** is in agreement with that obtained by the DMol^3 package, except that the band gap increase is smaller (the band gap increases by 0.04 eV relative to Δ_0 in our VASP calculation and 0.071 eV in our DMol^3 calculation for $E_\perp=-0.5$ V/Å). Therefore, we can conclude that a vertical external electric field is able to tune the band gap for Configurations **3**, **7** and **8**.

The effective masses of the holes (m_h) and electrons (m_e) in Configurations **1** and **3** are slightly anisotropic. The values of m_h and m_e are similar along the same direction as a result of an approximately symmetric dispersion of the conduction and the valence bands at the *K* point. The zero-field effective carrier masses for Configurations **1** and **3** are approximately equal, with values of $0.021m_0$ (where m_0 is the electron mass) along the Γ–*K* direction and $0.017m_0$ along the *K*–*M* direction, both of which are of the same order of magnitude as the measured m_e=$0.05m_0$ for the graphene/h-BN bilayer structure.[34] The effective carrier masses of Configuration **3** increase with the increasing band gap and reach $0.052m_0$ along the Γ–*K* direction at Δ_{max} (Figure 6). The measured carrier mobility of graphene on the h-BN substrate is comparable to that of suspended graphene, and it is one order of magnitude larger than that of SiO_2-supported graphene because the atomically flat h-BN substrate is free from dangling bonds and charge impurities.[14] It is reasonable to assume that the scattering time τ of the carriers in graphene sandwiched between h-BN layers is similar

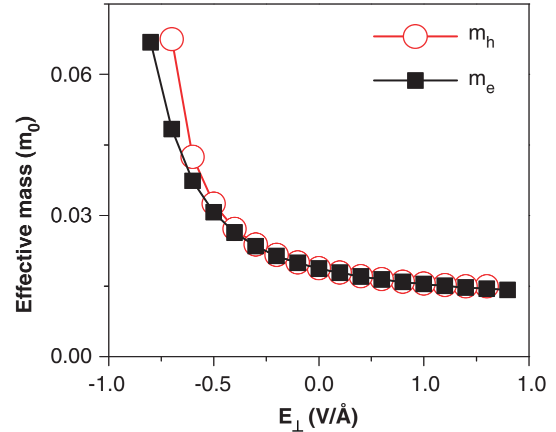

Figure 6 Carrier effective masses of Configuration **3** as a function of the electric field strength at the LDA/DNP level.

to that of suspended or h-BN-supported graphene. From the values of m_e=$0.021m_0$ and $\mu=2\times10^5$ cm^2 V^{-1} s^{-1} in the suspended BLG,[3] the zero-field carrier mobility in Configurations **1** and **3** is estimated to be $\mu\sim2\times10^5$ cm^2 V^{-1} s^{-1} along the Γ–*K* direction and $\sim2.5\times10^5$ cm^2 V^{-1} s^{-1} along the *K*–*M* direction, according to $\mu=e\tau/m$. The mobility at Δ_{max} of Configuration **3** is estimated to be $\mu_e\sim0.8\times10^5$ cm^2 V^{-1} s^{-1}.

GW approximation

We show the *GW* band structures for Configurations **1**, **3** and **11** in Figure 3 with red circles. Compared with the DFT band structures (DNP basis set and DMol^3 package) shown by blue lines in Figure 3, the band gaps increase from 0.115, 0.108 and 0.160 eV to 0.162, 0.158 and 0.232 eV, respectively, upon including the self-energy correction. The relative increases in the band gap are 41, 46 and 45% for Configurations **1**, **3** and **11**, respectively. To conduct a more proper comparison, we select the DFT band structures obtained with the same basis set (PW basis set) and package (ABINIT) as the *GW* calculation. For this comparison, the resulting relative increases are 57, 61 and 105%, which are comparable to or larger than that in graphene (59%).[19] The changes in the relative increases are smaller for Configurations **1** and **3,** but they are larger for Configuration **11** because the ABINIT package gives a smaller DFT band gap of 0.13 eV as a result of the larger interlayer distance of 3.51 Å (compared with a larger band gap of 0.16 eV and a smaller interlayer distance of 3.42 Å in the DMol^3 calculation).

Any successor to the silicon metal–oxide–semiconductor FET must have a large on/off ratio between 10^4 and 10^7, which requires the semiconducting channel with a sizeable band gap, preferably 0.4 eV or greater.[35] Given the similar correction ratio for the band gap under an electric field, the maximum quasiparticle band gaps of eight of the configurations will exceed 0.4 eV under a strong electric field and satisfy the requirement for a high-performance FET. In addition, the self-energy correction will slightly reduce the effective mass at the *K* point, thus increasing the carrier mobility slightly. The increase of the carrier mobility with the increasing band gap caused by self-energy correction is impressive because the carrier mobility usually decreases with the increasing band gap in terms of the effective mass theory.

Transport properties

The opening of a band gap in the h-BN/SLG/h-BN sandwich structures is reflected in the transport properties. We perform first-principles quantum transport calculations for the h-BN/SLG/h-BN

sandwich structures. The schematic model of a dual-gated FET based on Configuration **3** is shown in Figure 7a. The zero-bias transmission spectra of this device are displayed in Figures 7b and c. The inset in Figure 7b shows the transmission spectrum of SLG at zero bias, for which the gap at E_f is nearly zero. A transport gap of 0.037 eV is observed when SLG is sandwiched between h-BN in Configuration **3,** and the gap increases further to 0.26 eV under $E_{\perp}$=−1 V/Å. The two transport gaps are consistent with the corresponding band gaps of Δ_0=0.108 and 0.298 eV. Therefore, the electric-field-enhanced transport gap is well established for an h-BN/SLG/h-BN sandwich device. If the *GW* correction is considered, the calculated transport gap is expected to increase by more than 50%.

The existence of an appreciable transport gap in this vertically biased device suggests a switching effect controlled by a gate voltage, which suggests a device application. The transmission spectrum can be shifted by the gate voltage. Figure 7d shows the transmission spectra of this device under V_g=3.0 V and V_g=−6.0 V, with a fixed bias of 0.1 V and $E_{\perp}$=−1 V/Å. The transmission coefficients within the bias window under V_g=−6.0 V (on-state) are much larger than those under V_g=3.0 V (off-state). Figure 7e shows the corresponding transfer characteristic with a *p*-type feature. The on/off current ratio is 8.5, which is larger than the ratio of 1.06 exhibited by the pure SLG FET (inset of Figure 7e) by a factor of 8.0. This current switch effect is much weaker than that of a traditional metal oxide semiconductor

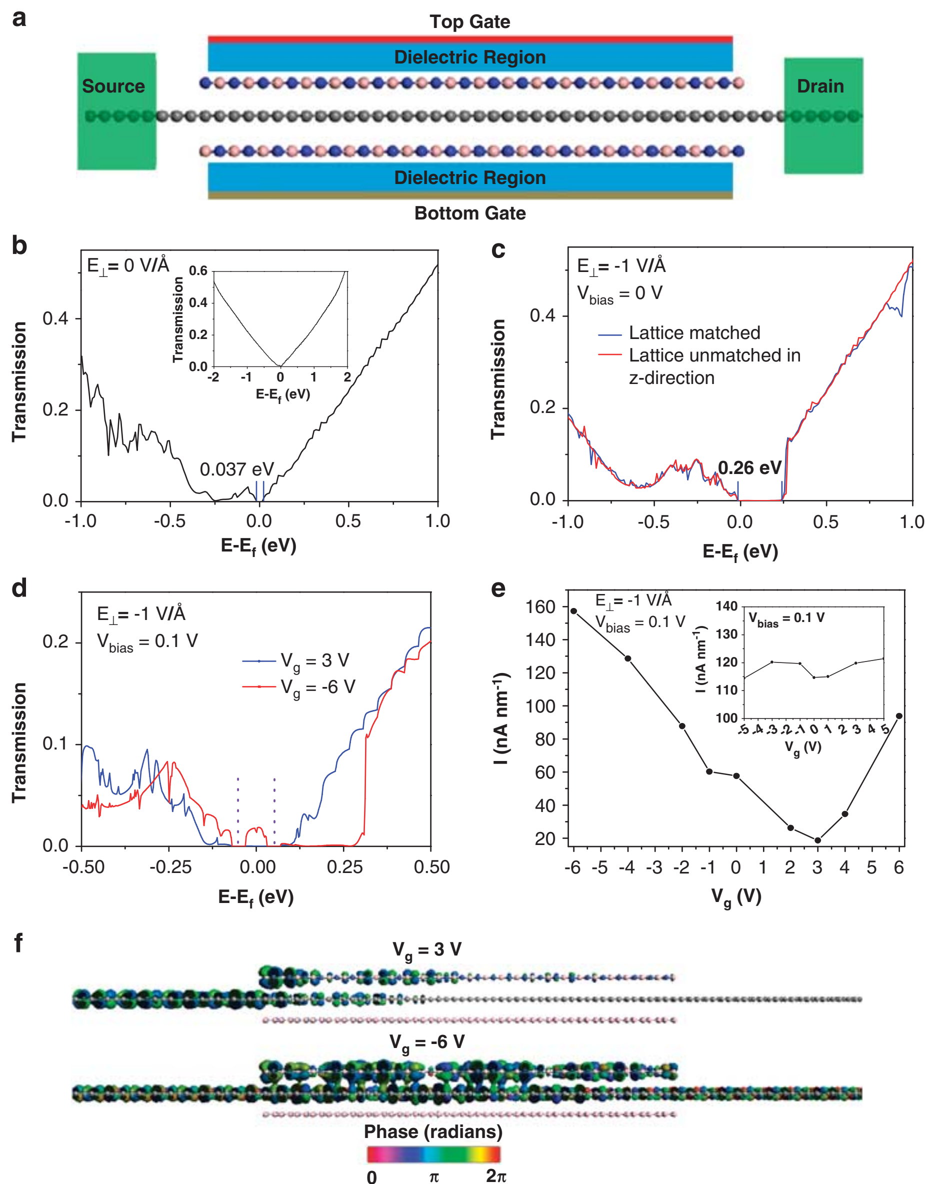

Figure 7 Dual-gated field effect transistor based on Configuration **3**. (**a**) Schematic model. The channel is 8.37 nm long, and the electrodes are composed of semi-planar graphene. Gray ball: C; blue ball: N; pink ball: B. (**b**) Transmission spectrum under $E_{\perp}$=0 V/Å. Inset: transmission spectrum of single-layer graphene at zero bias. (**c**) Transmission spectrum under $E_{\perp}$=−1 V/Å and V_{bias}=0 V. The blue and red curves represent the results of the lattice constants of single-layer h-BN and graphene matched and unmatched in the transport direction (*z*-direction), respectively. (**d**) Transmission spectrums of the off-state (V_g=3.0 V) and on-state (V_g=−6.0 V). The dashed vertical line indicates the bias window. (**e**) Transfer characteristic under V_{bias}=0.1 V and $E_{\perp}$=−1 V/Å. Inset: calculated transfer characteristic for a pure SLG FET under V_{bias}=0.1 V. (**f**) Transmission eigenstates of the off-state (V_g=3.0 V) and the on-state (V_g=−6.0 V) at E_f and at the (0, 1/3) point of the *k*-space under V_{bias}=0.1 V and $E_{\perp}$=−1 V/Å. The isovalue is 1.0 a.u.

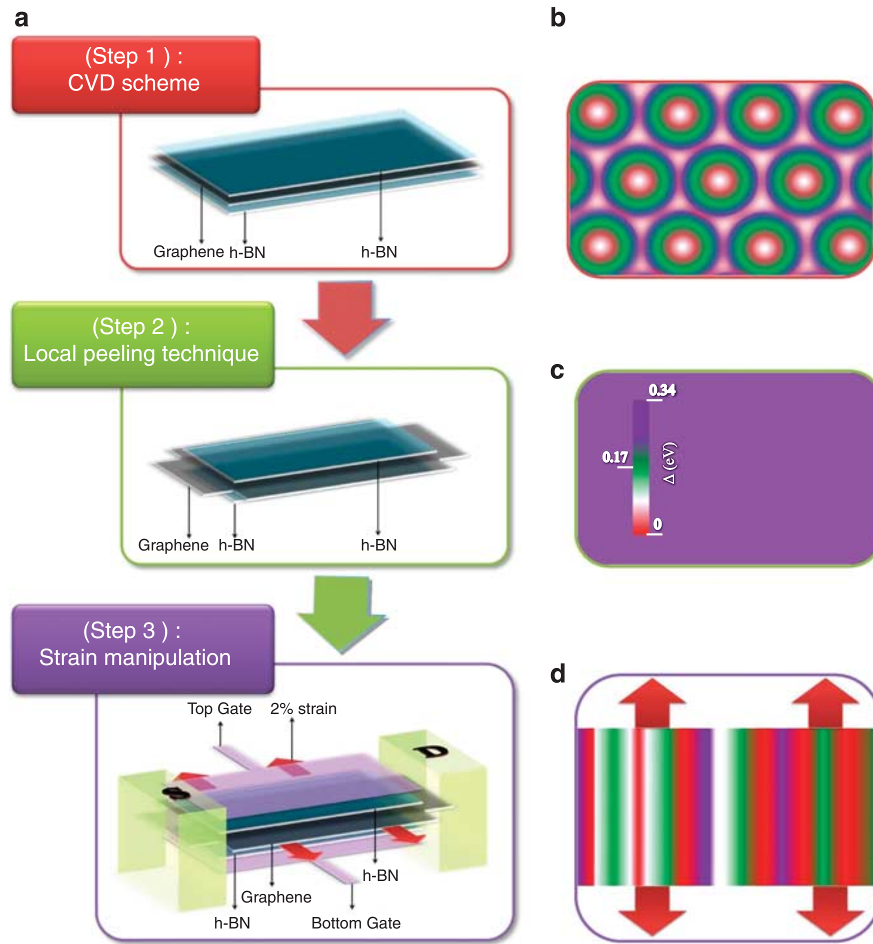

Figure 8 (**a**) Schematic illustration of a feasible solution for synthesis of the partial lattice-matched h-BN/SLG/h-BN sandwich device—Step 1: CVD growth of orientation-matched h-BN/SLG/h-BN sandwich. Step 2: exposure of four edges of SLG by local peeling. Step 3: two edges of SLG are used as source and drain, respectively, and the other two edged are stretched by 2%. Gray layer: graphene; blue layer: h-BN. (**b**–**d**) Spatial distribution of the band gaps in the sandwich device with (**b**) lattice mismatch, (**c**) total lattice match and (**d**) partial lattice match (along the *x*-direction).

FET.[35] However, it should be noted that one of the most striking merits of graphene and silicene (the silicon analog of graphene) is their extraordinary high carrier mobility. We must accept the compromised switching effect to maintain the extremely high carrier mobility of graphene and silicene.[31] The measured room-temperature on/off ratio of a vertically biased BLG FET is only increased by a factor of 25 over that of the unbiased FET at room temperature.[11] In our model, the on/off ratio can be further enhanced by adding a gate voltage to improve the on-current, because the on-current is well below its saturation value. The on/off ratio can also be further enhanced by device optimization techniques, such as increasing the channel length to decrease the off-state current leakage caused by tunneling.[31] Furthermore, the calculated transport gap is expected to increase by more than 50% when the *GW* correction is considered. As a result, the current leakage will be further decreased, and the on/off ratio will be increased.

The difference between the off-state and the on-state is reflected by the transmission eigenchannels at E_f and at the (0, 1/3) point of the *k*-space, as shown in Figure 7f. The transmission eigenvalue of the off-state is 4.66×10^{-3}, and the incoming wave function is almost completely scattered, so that it is unable to reach the other lead. In contrast, the transmission eigenvalue of the on-state is 0.99; the incoming wave function is scattered little; and most of the incoming wave is able to reach the other lead.

In these calculations, we assume that the lattice constants of SLG and h-BN are identical. In an actual h-BN/SLG/h-BN sandwich structure, a mismatch of the lattice constant is expected to cause variation of the stacking mode, leading to a spatial variation of the band gap. We relax the lattice constant of h-BN along the transport direction to consider the effects of partial lattice mismatch. The relaxed lattice constant of the h-BN is increased by 1.1% along the transport direction. The resulting zero-bias transmission spectrum under $E_{\perp}=-1$ V/Å is displayed in Figure 7c by the red line. Compared with the situation of matching lattices, the transmission spectrum shape is only slightly changed, and the transport gap is intact. When the lattice constant was mismatched along the transport direction, the band gap (and thus transport gap) of the sandwich varies along the transport direction, and the final transport gap depends on the maximum local transport gap caused by the series feature of the different local band gaps. In our case, the total transport gap of Configuration **3** remains unchanged upon lattice relaxation along the transport direction because Configuration **3** has a nearly maximal transport gap under $E_{\perp}=-1$ V/Å.

DISCUSSION

A well-defined orientation is necessary to open a local band gap in the examined h-BN/SLG/h-BN sandwich structures. Recently, the chemical vapor deposition (CVD) process has been used to grow graphene on a metal-substrate-supported h-BN single layer with either a strong[34] or weak[36,37] interaction between the h-BN single layer and the metal substrates and a well-defined orientation with respect to the h-BN layer.[34] Conversely, h-BN can also be grown on graphene by the CVD process.[38] We expect that h-BN/SLG/h-BN sandwiches with well-defined orientation could be synthesized by combining the two CVD schemes; therefore, the observation of a sizable local band gap in the h-BN/SLG/h-BN sandwich is anticipated.

However, the actual 2% mismatch between the graphene and the h-BN makes each stacking configuration appear with equal probability, and there is no sizable global band gap. To overcome this problem, new experimental approaches should be developed. In Figure 8, a feasible flow chart is proposed. First, as illustrated above, a sandwich structure with matched orientations between the graphene and the h-BN is obtained by combining the two CVD schemes. Second, by applying the local peeling technique developed by Dimiev *et al*.,[39] the four graphene edges of the sandwich structure can be exposed. Third, by exerting a homogeneous strain of 2% on the four sides of the graphene layer, a sandwich structure with matched lattice constants can be obtained. However, from the perspective of device performance, the fully lattice-matched sandwich structure is not necessarily favorable because the two most stable configurations only generate a band gap of <0.15 eV. Actually, the application of different strains on two layers of BLG has been suggested to open a band gap.[40] We suggest the exertion of a uniaxial strain of 2% on the two sides of the graphene layer along the x-direction (the direction in the plane of the graphene layer but perpendicular to the transport z-direction) and matching of the lattice constants of the h-BN and graphene in this direction. Different local band gaps will appear in the transport direction (Figure 8c), but the final transport gap depends on the largest local band gap (more than 0.3 eV under a strong electric field) of the h-BN/SLG/h-BN sandwich because of the series feature of the different local band gaps. Therefore, the partially lattice-matched sandwich exhibits better device performance. A similar example is the transport gap of a graphene nanoribbon (GNR). An experiment performed by Dai *et al*.[4] found that sub-10-nm GNRs always have a transport gap. This result appears strange because both armchair and zigzag GNRs should exist. Armchair GNRs are semiconducting, but zigzag GNRs prefer a metallic state at room temperature. The most probable reason for the occurrence of this gap is the nonuniformity of the edges of the GNRs, so that both armchair and zigzag edges coexist in a single GNR, and the transport gap of the GNRs actually depends on the local band gap of the armchair edge.

In conclusion, by using DFT calculations, we demonstrate that the effects of a vertical electric field on the electronic structure of an h-BN/SLG/h-BN sandwich structure depend on the mode of stacking. An optimally stacked h-BN/SLG/h-BN sandwich structure can have both a sizable band gap and a high carrier mobility under a strong electric field. Many-body effects enhance the band gap of the h-BN/SLG/h-BN sandwich system by more than 50%. A sizable transport gap, which is comparable with the band gap, and an enhancement in the switching effect with respect to that of pure SLG FET are observed in the *ab initio* transport simulation of a dual-gated sandwich structure FET. We anticipate that our work will stimulate the synthesis of an h-BN/SLG/h-BN sandwich that will produce remarkable performance in further nanoelectronic applications.

ACKNOWLEDGEMENTS

We thank Prof J Kong and Prof J Zhang for helpful discussions. This work was supported by the NSFC (Grant No. 10774003), National 973 Projects (No. 2007CB936200, MOST of China), Program for New Century Excellent Talents in University of MOE, Fundamental Research Funds for the Central Universities, National Foundation for Fostering Talents of Basic Science (No. J0630311) of China, Grant–in–Aid for Next Generation Super Computing Project (Nanoscience Program), and Specially Promoted Research from the MEXT in Japan, and Nebraska Research Initiative and DOE DE-EE0003174 in the United States.

1 Novoselov, K. S., Geim, A. K., Morozov, S. V., Jiang, D., Katsnelson, M. I., Grigorieva, I. V., Dubonos, S. V. & Firsov, A. A. Two-dimensional gas of massless dirac fermions in graphene. *Nature* **438,** 197–200 (2005).
2 Du, X., Skachko, I., Barker, A. & Andrei, E. Y. Approaching ballistic transport in suspended graphene. *Nat. Nanotech.* **3,** 491–495 (2008).
3 Morozov, S. V., Novoselov, K. S., Katsnelson, M. I., Schedin, F., Elias, D. C., Jaszczak, J. A. & Geim, A. K. Giant intrinsic carrier mobilities in graphene and its bilayer. *Phys. Rev. Lett.* **100,** 016602 (2008).
4 Wang, X. R., Ouyang, Y. J., Li, X. L., Wang, H. L. & Dai, H. J. Room-temperature all-semiconducting sub-10-nm graphene nanoribbon field-effect transistors. *Phys. Rev. Lett.* **100,** 206803 (2008).
5 Bai, J. W., Zhong, X., Jiang, S., Huang, Y. & Duan, X. F. Graphene nanomesh. *Nat. Nanotech.* **5,** 190–194 (2010).
6 Balog, R., Jørgensen, B., Nilsson, L., Andersen, M., Rienks, E., Bianchi, M., Fanetti, M., Lægsgaard, E., Baraldi, A., Lizzit, S., Sljivancanin, Z., Besenbacher, F., Hammer, B., Pedersen, T. G., Hofmann, P. & Hornekær, L. Bandgap opening in graphene induced by patterned hydrogen adsorption. *Nat. Mater.* **9,** 315–319 (2010).
7 Withers, F., Dubois, M. & Savchenko, A. K. Electron properties of fluorinated single-layer graphene transistors. *Phys. Rev. B* **82,** 073403 (2010).
8 Zhou, S. Y., Gweon, G. H., Fedorov, A. V., First, P. N., De Heer, W. A., Lee, D. H., Guinea, F., Castro Neto, A. H. & Lanzara, A. Substrate-induced bandgap opening in epitaxial graphene. *Nat. Mater.* **6,** 770–775 (2007).
9 Giovannetti, G., Khomyakov, P. A., Brocks, G., Kelly, P. J. & van den Brink, J. Substrate-induced band gap in graphene on hexagonal boron nitride: *Ab initio* density functional calculations. *Phys. Rev. B* **76,** 073103 (2007).
10 Choi, S.- M., Jhi, S.- H. & Son, Y.- W. Effects of strain on electronic properties of graphene. *Phys. Rev. B* **81,** 081407 (2010).
11 Xia, F. N., Farmer, D. B., Lin, Y.- M. & Avouris, P. Graphene field-effect transistors with high on/off current ratio and large transport band gap at room temperature. *Nano Lett.* **10,** 715–718 (2010).
12 Zhang, Y. B., Tang, T. T., Girit, C., Hao, Z., Martin, M. C., Zettl, A., Crommie, M. F., Shen, Y. R. & Wang, F. Direct observation of a widely tunable bandgap in bilayer graphene. *Nature* **459,** 820–823 (2009).
13 Oostinga, J. B., Heersche, H. B., Liu, X. L., Morpurgo, A. F. & Vandersypen, L. M. K. Gate-induced insulating state in bilayer graphene devices. *Nat. Mater.* **7,** 151–157 (2008).
14 Dean, C. R., Young, A. F., Meric, I., Lee, C., Wang, L., Sorgenfrei, S., Watanabe, K., Taniguchi, T., Kim, P., Shepard, K. L. & Hone, J. Boron nitride substrates for high-quality graphene electronics. *Nat. Nanotech.* **5,** 722–726 (2010).
15 Sławińska, J., Zasada, I., Kosiński, P. & Klusek, Z. Reversible modifications of linear dispersion: graphene between boron nitride monolayers. *Phys. Rev. B* **82,** 085431 (2010).
16 Ramasubramaniam, A., Naveh, D. & Towe, E. Tunable band gaps in bilayer graphene/h-BN heterostructures. *Nano Lett.* **11,** 1070–1075 (2011).
17 Yang, L., Deslippe, J., Park, C.- H., Cohen, M. L. & Louie, S. G. Excitonic effects on the optical response of graphene and bilayer graphene. *Phys. Rev. Lett.* **103,** 186802 (2009).
18 Wirtz, L., Marini, A. & Rubio, A. Excitons in boron nitride nanotubes: dimensionality effects. *Phys. Rev. Lett.* **96,** 126104 (2006).
19 Cudazzo, P., Attaccalite, C., Tokatly, I. V. & Rubio, A. Strong charge-transfer excitonic effects and the bose-einstein exciton condensate in graphane. *Phys. Rev. Lett.* **104,** 226804 (2010).
20 Delley, B. An all-electron numerical-method for solving the local density functional for polyatomic-molecules. *J. Chem. Phys.* **92,** 508–517 (1990).
21 Delley, B. From molecules to solids with the $DMol^3$ approach. *J. Chem. Phys.* **113,** 7756–7764 (2000).
22 Monkhorst, H. J. & Pack, J. D. Special points for brillouin-zone integrations. *Phys. Rev. B* **13,** 5188 (1976).
23 Baskin, Y. & Meyer, L. Lattice constants of graphite at low temperatures. *Phys. Rev.* **100,** 544 (1955).
24 Kresse, G. & Joubert, D. From ultrasoft pseudopotentials to the projector augmented-wave method. *Phys. Rev. B* **59,** 1758 (1999).
25 Gonze, X., Amadon, B., Anglade, P. M., Beuken, J. M., Bottin, F., Boulanger, P., Bruneval, F., Caliste, D., Caracas, R., Côté, M., Deutsch, T., Genovese, L., Ghosez, P., Giantomassi, M., Goedecker, S., Hamann, D. R., Hermet, P., Jollet, F., Jomard, G., Leroux, S., Mancini, M., Mazevet, S., Oliveira, M. J. T., Onida, G., Pouillon, Y., Rangel, T., Rignanese, G. M., Sangalli, D., Shaltaf, R., Torrent, M., Verstraete, M. J., Zerah, G. & Zwanziger, J. W. ABINIT: first-principles approach to materials and nanosystem properties. *Comput. Phys. Commun.* **180,** 2582–2615 (2009).

26 Torrent, M., Jollet, F., Bottin, F., Zerah, G. & Gonze, X. Implementation of the projector augmented-wave method in the ABINIT code. *Comp. Mater. Sci.* **42,** 337 (2008).
27 Onida, G., Reining, L. & Rubio, A. Electronic excitations: density-functional versus many-body green's-function approaches. *Rev. Mod. Phys.* **74,** 601–659 (2002).
28 Bruneval, F. & Gonze, X. Accurate *GW* self-energies in a plane-wave basis using only a few empty states: towards large systems. *Phys. Rev. B* **78,** 085125 (2008).
29 Brandbyge, M., Mozos, J., Luis, O., Pablo, O., Taylor, J. & Stokbro, K. Density-functional method for nonequilibrium electron transport. *Phys. Rev. B* **65,** 165401 (2002).
30 Soler, J. M., Artacho, E., Gale, J. D., García, A., Junquera, J., Ordejón, P. & Sánchez-Portal, D. The SIESTA method for *ab initio* order-N materials simulation. *J. Phys.: Condens. Matter.* **14,** 2745 (2002).
31 Ni, Z. Y., Liu, Q. H., Tang, K. C., Zheng, J. X., Zhou, J., Qin, R., Gao, Z. X., Yu, D. P. & Lu, J. Tunable bandgap in silicene and germanene. *Nano Lett.* **12,** 113–118 (2012).
32 Xu, Y. H., Li, X. W. & Dong, J. M. Infrared and Raman spectra of AA-stacking bilayer graphene. *Nanotechnology* **21,** 065711 (2010).
33 Sławińska, J., Zasada, I. & Klusek, Z. Energy gap tuning in graphene on hexagonal boron nitride bilayer system. *Phys. Rev. B* **81,** 155433 (2010).
34 Bjelkevig, C., Mi, Z., Xiao, J., Dowben, P. A., Wang, L., Mei, W.- N. & Kelber, J. A. Electronic structure of a graphene/hexagonal-BN heterostructure grown on Ru(0001) by chemical vapor deposition and atomic layer deposition: extrinsically doped graphene. *J. Phys.: Condens. Matter.* **22,** 302002 (2010).
35 Schwierz, F. Graphene transistors. *Nature Nanotech.* **5,** 487–496 (2010).
36 Usachov, D., Adamchuk, V. K., Haberer, D., Grüneis, A., Sachdev, H., Preobrajenski, A. B., Laubschat, C. & Vyalikh, D. V. Quasifreestanding single-layer hexagonal boron nitride as a substrate for graphene synthesis. *Phys. Rev. B* **82,** 075415 (2010).
37 Ding, X. L., Ding, G. Q., Xie, X. M., Huang, F. Q. & Jiang, M. H. Direct growth of few layer graphene on hexagonal boron nitride by chemical vapor deposition. *Carbon* **49,** 2522–2525 (2011).
38 Liu, Z., Song, L., Zhao, S. Z., Huang, J. Q., Ma, L. L., Zhang, J. N., Lou, J. & Ajayan, P. M. Direct growth of graphene/hexagonal boron nitride stacked layers. *Nano Lett.* **11,** 2032–2037 (2011).
39 Dimiev, A., Kosynkin, D. V., Sinitskii, A., Slesarev, A., Sun, Z. & Tour, J. M. Layer-by-layer removal of graphene for device patterning. *Science* **331,** 1168–1172 (2011).
40 Choi, S.- M., Jhi, S.- H. & Son, Y.- W. Controlling energy gap of bilayer graphene by strain. *Nano Lett.* **10,** 3486–3489 (2010).

This work is licensed under the Creative Commons Attribution-NonCommercial-No Derivative Works 3.0 Unported License. To view a copy of this license, visit http://creativecommons.org/licenses/by-nc-nd/3.0/

Supplementary Information accompanies the paper on the NPG Asia Materials website (http://www.nature.com/am)